fractal and fractional

MDPI

Article

A Novel Softsign Fractional-Order Controller Optimized by an Intelligent Nature-Inspired Algorithm for Magnetic Levitation Control

Davut Izci [1,2], Serdar Ekinci [3], Mohd Zaidi Mohd Tumari [4] and Mohd Ashraf Ahmad [5,*]

[1] Department of Electrical and Electronics Engineering, Bursa Uludag University, Bursa 16059, Turkey; davutizci@uludag.edu.tr
[2] Applied Science Research Center, Applied Science Private University, Amman 11931, Jordan
[3] Department of Computer Engineering, Bitlis Eren University, Bitlis 13100, Turkey; sekinci@beu.edu.tr
[4] Faculty of Electrical Engineering Technology, Universiti Teknikal Malaysia Melaka, Durian Tunggal 76100, Melaka, Malaysia; mohdzaidi.tumari@utem.edu.my
[5] Faculty of Electrical and Electronics Engineering Technology, Universiti Malaysia Pahang Al-Sultan Abdullah, Pekan 26600, Pahang, Malaysia
* Correspondence: mashraf@ump.edu.my

Abstract

This study presents a novel softsign-function-based fractional-order proportional–integral–derivative (softsign-FOPID) controller optimized using the fungal growth optimizer (FGO) for the stabilization and precise position control of an unstable magnetic ball suspension system. The proposed controller introduces a smooth nonlinear softsign function into the conventional FOPID structure to limit abrupt control actions and improve transient smoothness while preserving the flexibility of fractional dynamics. The FGO, a recently developed bio-inspired metaheuristic, is employed to tune the seven controller parameters by minimizing a composite objective function that simultaneously penalizes overshoot and tracking error. This optimization ensures balanced transient and steady-state performance with enhanced convergence reliability. The performance of the proposed approach was extensively benchmarked against four modern metaheuristic algorithms (greater cane rat algorithm, catch fish optimization algorithm, RIME algorithm and artificial hummingbird algorithm) under identical conditions. Statistical analyses, including boxplot comparisons and the nonparametric Wilcoxon rank-sum test, demonstrated that the FGO consistently achieved the lowest objective function value with superior convergence stability and significantly better ($p < 0.05$) performance across multiple independent runs. In time-domain evaluations, the FGO-tuned softsign-FOPID exhibited the fastest rise time (0.0089 s), shortest settling time (0.0163 s), lowest overshoot (4.13%), and negligible steady-state error (0.0015%), surpassing the best-reported controllers in the literature, including the sine cosine algorithm-tuned PID, logarithmic spiral opposition-based learning augmented hunger games search algorithm-tuned FOPID, and manta ray foraging optimization-tuned real PIDD^2. Robustness assessments under fluctuating reference trajectories, actuator saturation, sensor noise, external disturbances, and parametric uncertainties ($\pm$10% variation in resistance and inductance) further confirmed the controller's adaptability and stability under practical non-idealities. The smooth nonlinearity of the softsign function effectively prevented control signal saturation, while the fractional-order dynamics enhanced disturbance rejection and memory-based adaptability. Overall, the proposed FGO-optimized softsign-FOPID controller establishes a new benchmark in nonlinear magnetic levitation control by integrating smooth nonlinear mapping, fractional calculus, and adaptive metaheuristic optimization.

check for updates

Academic Editor: David Kubanek

Received: 24 October 2025
Revised: 2 December 2025
Accepted: 5 December 2025
Published: 7 December 2025

Citation: Izci, D.; Ekinci, S.; Mohd Tumari, M.Z.; Ahmad, M.A. A Novel Softsign Fractional-Order Controller Optimized by an Intelligent Nature-Inspired Algorithm for Magnetic Levitation Control. *Fractal Fract.* **2025**, *9*, 801. https://doi.org/10.3390/fractalfract9120801

Keywords: fungal growth optimizer; softsign function-based FOPID controller; unstable magnetic ball suspension system; robustness; AI-based algorithms

1. Introduction

Magnetic levitation (Maglev) systems have long served as canonical benchmarks in modern control engineering due to their intrinsic nonlinearity, open-loop instability, and sensitivity to parameter variations. Among these, the magnetic-ball suspension (MBS) configuration represents a classical and experimentally tractable example, wherein a steel ball is levitated by an electromagnetic actuator without mechanical contact. Such systems are inherently unstable because the electromagnetic force depends nonlinearly on coil current and ball position, requiring continuous feedback control to maintain equilibrium [1]. Achieving robust and precise levitation remains a critical challenge that continues to motivate the development of advanced control strategies [2].

Historically, the control of Maglev systems began with classical linear techniques such as proportional–integral–derivative (PID) controllers because of their conceptual simplicity and ease of real-time implementation [3,4]. However, linear PID designs often struggle with the strong nonlinearity of electromagnetic actuation, leading to high overshoot, long settling times, and inadequate robustness under parameter drift or external disturbances [5]. Consequently, researchers proposed various extensions of PID control, including the proportional–integral–derivative–acceleration (PIDA) and real PIDD^2 structures [6,7]. Multi-degree-of-freedom (2-DOF and 3-DOF) PID variants were also developed to improve decoupling between reference tracking and disturbance rejection [8].

Parallel to these developments, fractional-order control emerged as a powerful paradigm for nonlinear dynamic systems. Fractional-order PID (FOPID) controllers, characterized by non-integer integration and differentiation orders (λ, μ), provide an additional degree of tuning flexibility and can emulate memory and hereditary properties absent in integer-order counterparts. Experimental and simulation studies have demonstrated that FOPID improves robustness and disturbance rejection for Maglev and electromagnetic suspension systems [9–11].

In addition to fractional-order control, researchers have explored a wide range of nonlinear and adaptive control strategies, including fuzzy PID [12], neural-network-based control [13], adaptive neuro-fuzzy inference systems (ANFISs) [14], sliding-mode control (SMC) [15], model-predictive control (MPC) [16], model-reference adaptive control (MRAC) [17], and cascaded or lead–lag compensators [18]. Each method offers improvements in adaptability or robustness but frequently entails higher computational demand and more intricate tuning.

The current literature can broadly be categorized into three methodological clusters: (1) classical and multi-DOF PID controllers, (2) fractional-order and nonlinear PID architectures and (3) optimization-driven intelligent controllers. Studies related to real PIDD^2 [19] and 2-DOF PID [20] structures achieve improved transient performance and phase compensation. However, their robustness remains limited under strong nonlinearity. FOPID controllers [21] were shown to outperform integer PIDs in both stability margins and control effort. Nonlinear augmentations (including fuzzy PID, sigmoid PID, and exponential PID) have been introduced to improve control smoothness [22–24].

The integration of metaheuristic algorithms has revolutionized tuning practices for nonlinear control. Algorithms such as particle swarm optimization (PSO) [25], genetic algorithm (GA) [26], differential evolution (DE) [27], manta ray foraging optimization (MRFO) [19], hunger games search (HGS) [28], and its hybrid version [28] have been

applied to optimize PID or FOPID parameters for maglev systems, leading to significant performance improvements.

Across these clusters, two key observations emerge. First, while FOPID controllers exhibit enhanced robustness, most existing designs rely on linear or discontinuous nonlinear functions within the control law. These can cause abrupt control actions or chattering during large transients. Nonlinear variants (fuzzy or sigmoid PID) attempt to smooth control responses but often introduce asymmetrical mappings or high computational cost [29]. There remains an absence of smooth, bounded, and differentiable nonlinear functions (such as the softsign activation function) integrated directly into the FOPID structure for maglev control. Second, the performance of optimization-based controllers largely depends on the algorithm's exploration–exploitation balance. Conventional algorithms such as PSO, DE, or SCA may converge prematurely or show inconsistent results in high-dimensional spaces [22,30]. More recent adaptive optimizers, including the fungal growth optimizer (FGO), inspired by hyphal tip extension, chemotropism, and branching behaviors of fungi, demonstrate dynamic self-adaptation and have achieved superior convergence in engineering optimization tasks [31]. However, no published study has reported the application of FGO for controller tuning in maglev or similar unstable nonlinear systems. Hence, two intertwined research gaps are evident: (1) the absence of a smoothly nonlinear fractional-order controller for maglev systems, and (2) the unexplored potential of FGO-based tuning for robust control optimization.

To address these gaps, this study proposes a softsign fractional-order PID (Softsign-FOPID) controller, optimized via the FGO, for precise and robust control of the magnetic-ball suspension system. The softsign function provides a bounded and continuously differentiable nonlinearity that smooths control signals while preserving steady-state accuracy. The FGO algorithm ensures adaptive and consistent convergence by balancing global exploration and local exploitation. The main contributions are as follows considering the above discussion:

- A first-of-its-kind controller architecture, embedding a softsign nonlinear function within a FOPID structure for Maglev systems.
- Integration of the fungal growth optimizer (FGO) for controller tuning—its first reported use in control-system optimization.
- Formulation of a composite objective function that penalizes both overshoot and integrated absolute error (IAE), ensuring a trade-off between transient and steady-state behavior.
- A comprehensive comparative analysis against contemporary optimizers (GCRA, CFOA, RIME, AHA) and leading literature benchmarks demonstrating superior performance and robustness under fluctuating reference inputs, actuator saturation, external disturbances, and parameter uncertainties.

The remainder of the paper is organized as follows: Section 2 explains the FGO algorithm. Section 3 models the magnetic-ball suspension system. Section 4 details the Softsign-FOPID controller design and objective-function formulation. Section 5 presents optimization results and comparative analyses. Section 6 evaluates robustness under non-ideal conditions. Section 7 concludes the work and outlines future research perspectives.

2. Fungal Growth Optimizer

Fungal growth optimizer (FGO) [31] is a recent metaheuristic algorithm inspired by the adaptive behaviors of fungi in nature, particularly hyphal tip extension, chemotropic movement, and branching mechanisms. These behaviors allow fungi to explore and exploit their environment efficiently, making FGO a powerful framework for solving complex, nonlinear optimization problems. FGO starts by initializing a population of agents called hyphae, each representing a candidate solution. The initial positions of these

hyphae are randomly generated across the defined search space using Equation (1) where $i = 1, 2, \ldots, N$.

$$\vec{S}_i^0 = \vec{S}_L + r \odot \left(\vec{S}_U - \vec{S}_L \right) \tag{1}$$

Here, $\vec{S}_L$ and $\vec{S}_U$ are the lower and upper bounds of the search space, and $r \in [0,1]^d$ is a uniformly distributed random vector. Each hypha then undergoes an iterative growth process. At each iteration t, a hypha may either continue growth along its tip, branch laterally, or initiate a new germination depending on its relative performance and a set of stochastic rules.

Exploration in FGO is modeled through directional extension of hyphae toward diverse regions of the search space. The extension is driven by a growth rate E computed by Equation (2):

$$E = exp\left(\frac{f_i}{\sum_{j=1}^{N} f_j} \right) \times r_1 \times \left(1 - \frac{t}{t_{max}} \right)^{(1 - \frac{t}{t_{max}})} \tag{2}$$

where f_i denotes the fitness of the i-th solution, r_1 is a uniformly distributed random number in $[0,1]$ and t_{max} is the maximum number of iterations. The new direction $\vec{D}$ is defined by the difference between two randomly selected solution vectors:

$$\vec{D} = \vec{S}_a^t - \vec{S}_b^t \tag{3}$$

Then, the position is updated as in Equation (4).

$$\vec{S}_i^{t+1} = \vec{S}_i^t + E \times \vec{D} \tag{4}$$

To enhance exploration selectively in dimensions, a probabilistic filtering mechanism updates only certain components of the position vector (Equation (5)):

$$\vec{S}_{i,j}^{t+1} = \begin{cases} \vec{S}_{i,j}^{t+1}, & if\ R_j > r_3 \\ \vec{S}_{i,j}^{t}, & otherwise \end{cases} \qquad for\ j = 1, \ldots, d \tag{5}$$

where $R_j \sim \mathcal{U}(0,1)$ is the random number for the jth dimension and $r_3 \in [0,1]$ is a threshold value.

In the FGO, exploitation is modeled based on the chemotropism behavior of fungal hyphae, which enables directional growth toward favorable nutrient sources. This is mathematically expressed by Equation (6):

$$\vec{D}_i^e = r_4 \times \left(\vec{S}_a^t - \vec{S}_i^t \right) + r_5 \odot \left(\beta \times \vec{S}^* - \vec{S}_i^t \right) [r_6 > R] \tag{6}$$

where $\vec{S}_i^t$ is the current solution, $\vec{S}_a^t$ is a randomly selected solution from the population, $\vec{S}^*$ is the global best solution found so far, $r_4, r_5, r_6 \in [0,1]$ are random values generated from a uniform distribution, $\beta \in \{-1, +1\}$, is a direction control coefficient randomly chosen, $R \in [0,1]$ is a predefined threshold constant and $[r_6 > R]$ is evaluated as in Equation (7).

$$[r_6 > R] = \begin{cases} 1, & if\ r_6 > R \\ 0, & otherwise \end{cases} \tag{7}$$

This operator balances random directional movement (first term) with greedy attraction to the global best (second term), but the latter is only activated when $r_6 > R$, providing

conditional exploitation that enhances adaptability and avoids premature convergence. To adjust the aggressiveness of exploitation, an adaptive step size η_i is defined in Equation (8):

$$\eta_i = \begin{cases} r_7\,, & if\ t < \frac{t_{max}}{2} \\ \frac{\eta_i}{\sum_{k=1}^{N}\eta_k} + 2r_8, & otherwise \end{cases}, \qquad i = 1,\ 2,\ \ldots,\ N \tag{8}$$

where r_7 and r_8 are random numbers between 0 and 1. The position update rule incorporates both directional movement and a local perturbation vector $\vec{E}_c$:

$$\begin{gathered} \vec{S}_i^{t+1} = \vec{S}_i^{t} + \eta_i \times \vec{D}_i^{e} + \vec{E}_c \times \left[r_{12} > E_p\right] \\ \vec{E}_c = (r_9 - 0.5) \times r_{10} \odot \left(\vec{S}_a^{t} - \vec{S}_b^{t}\right) \end{gathered}, \ \left[r_{12} > E_p\right] = \begin{cases} 1, & if\ r_{12} > E_p \\ 0, & otherwise \end{cases} \tag{9}$$

where $E_p \in [0,1]$ is a fixed perturbation probability threshold and r_{12} is a random number. $\vec{S}_a^{t}$ and $\vec{S}_b^{t}$ are two distinct solutions. A greedy selection strategy is adopted as given in Equation (10) where $i = 1,2,\ldots,N$ and r_9, $r_{10}, r_{11}, r_{12} r_{13} r_{14} \in [0,1]$ are random scaling factors.

$$\vec{S}_i^{t+1} = \begin{cases} \vec{S}_i^{t} + \eta_i \times \vec{D}_i^{e2} + \vec{E}_c \times [r_{11} > r_{13}], & r_{14} < r_{15} \\ \vec{S}_i^{t} + \eta_i \times \vec{D}_i^{e} + \vec{E}_c \times \left[r_{12} > E_p\right], & else \end{cases} \tag{10}$$

To balance exploration and exploitation adaptively, each individual is assigned an exploration probability given in Equation (11):

$$p_i = \frac{f_i - f_{min}}{f_{max} - f_{min} + \varepsilon} \tag{11}$$

where f_{min} and f_{max} denote the best and worst fitness values in the current population, ε is a small constant to avoid division by zero. An adaptive factor controlling exploration pressure is defined by Equation (12):

$$E_r = \mathcal{M} - (1 + \mathcal{M}) \times \left(1 - \frac{t}{t_{max}}\right) \tag{12}$$

where $\mathcal{M} \in [0,1]$ is a constant controlling minimum exploitation pressure.

In the later stage of fungal evolution, when the growth of a hypha becomes unstable or encounters stressors such as nutrient deficiency or external environmental perturbations, the hypha may branch or germinate spores to enhance exploration and adaptation. To begin with, two directional growth patterns are considered for generating new hyphae. The first pattern is based on the difference between two randomly selected individuals from the population (Equation (13)).

$$\vec{D}_i^{ep1} = \left(\vec{S}_a^{t} - \vec{S}_b^{t}\right) \text{ and } \vec{D}_i^{ep2} = \left(\vec{S}_c^{t} - \vec{S}^{*}\right) \tag{13}$$

The direction of the new hypha is then determined by combining these two patterns based on a uniformly distributed random number r_5.

$$\vec{S}_i^{t+1} = \vec{S}_i^{t} + r_5 \times \vec{D}_i^{ep1} + (1 - r_5) \times \vec{D}_i^{ep2} \tag{14}$$

To account for growth dynamics under varying environmental conditions, the lateral growth rate is defined as in Equation (15):

$$E^L = 1 + e^{\frac{f_i}{\sum_{k=1}^{N} f_k}} \times [r_6 < r_7] \tag{15}$$

where f_k denotes the fitness value of the k-th individual. The Iverson bracket $[r_6 < r_7]$ equals 1 if the condition is true, and 0 otherwise. Using this dynamic growth rate, the updated lateral branching position for each dimension $j = 1, 2, \ldots, d$ is formulated as:

$$S_{i,j}^{t+1} = \left[R_j < r_3\right] \times S_{i,j}^t + \left(1 - \left[R_j < r_3\right]\right) \times \left(S_{i,j}^t + r_5 \times E^L \times D_i^{ep1} + (1 - r_5) \times E^L \times D_i^{ep2}\right) \tag{16}$$

where $R_j \in [0, 1]$ is a uniformly distributed random value for the j-th dimension. The model also introduces a spore germination mechanism to increase solution diversity. A new hypha is generated using the absolute difference between the mean of three randomly selected individuals and the current solution. Let $S_{a,j}^t$, $S_{b,j}^t$, $S_{c,j}^t$ denote randomly chosen individuals; then the spore germination update rule is given by Equation (17).

$$S_{i,j}^{t+1} = \left[R_j < r_3\right] \times S_{i,j}^t + \left(1 - \left[R_j < r_3\right]\right) \times \left(\frac{\left(\frac{\left(\left(\frac{t}{t_{max}}\right) \times S_j^* + \left(1 - \frac{t}{t_{max}}\right) \times S_{a,j}^t \right)}{2} + \overrightarrow{S}_b^t \right)}{2} + S_g \times r_5 \times E \times \left| \frac{S_{a,j}^t + S_{b,j}^t + S_{c,j}^t}{3} - S_{i,j}^t \right| \right) \tag{17}$$

Here, $S_g \in \{-1, +1\}$ is a randomly selected sign that dictates the direction of spore movement, and is the exponential growth rate parameter. Finally, the trade-off between branching and spore germination is determined stochastically. With 50% probability, one of the two perturbation strategies is applied via Equation (18).

$$\overrightarrow{S}_i^{t+1} = \begin{cases} Apply\ Equation\ (16) & r_7 < 0.5 \\ Apply\ Equation\ (17), & else \end{cases} \tag{18}$$

The pseudocode in Figure 1 provides the working principle of FGO explained above.

```
Input:
    Objective function
    Population size, search space dimension
    Maximum iteration
    Lower and upper bounds
    Algorithm parameters

Output:
    Best solution and its fitness
-----------------------------------------------------------
1. Initialization:
    For each hypha i = 1 to N:
        Initialize position using Eq. (1)
        Evaluate fitness
    Determine the best solution with minimum fitness
-----------------------------------------------------------
2. Main loop (for t = 1 to Maximum iteration):
    2.1 Hyphal Tip Growth (Exploration phase):
        For each hypha i:
            Compute growth rate using Eq. (2)
            Determine directional vector using Eq. (3)
            Update position according to Eq. (4)
            Apply selective dimension update following Eq. (5)
    2.2 Chemotropism Behavior (Exploitation phase):
        For each hypha i:
            Calculate direction of chemotropic movement using Eq. (6)
            Evaluate the conditional activation rule as in Eq. (7)
            Adapt step size according to Eq. (8)
            Compute perturbation vector and update position via Eq. (9)
            Apply greedy selection rule as defined in Eq. (10)
    2.3 Adaptive Control Mechanisms:
        Compute exploration probability using Eq. (11)
        Adjust exploration–exploitation balance by Eq. (12)
    2.4 Hyphal Branching and Spore Germination:
        For each hypha i:
            Generate exploration directions using Eq. (13)
            Combine directional patterns via Eq. (14)
            Calculate lateral growth rate following Eq. (15)
            Update branching positions selectively based on Eq. (16)
            Perform spore germination process according to Eq. (17)
            Choose between branching or germination following Eq. (18)
    2.5 Fitness Evaluation and Best Solution Update:
        Evaluate all new hyphae
        Update best solution if any better fitness value is obtained
-----------------------------------------------------------
3. Termination:
    Return best solution and fitness value
```

Figure 1. Pseudocode of FGO.

3. Mathematical Model of the Magnetic Ball Suspension System

The magnetic ball suspension system, schematically illustrated in Figure 2, is a classical nonlinear and open-loop-unstable benchmark plant widely used to validate advanced control strategies [19,32–34]. The configuration consists of an electromagnet, a steel ball, and associated circuitry containing a coil of resistance R and inductance L. The system operates by regulating the electromagnetic force that counteracts the gravitational pull acting on the steel ball, thereby maintaining a desired levitation height y.

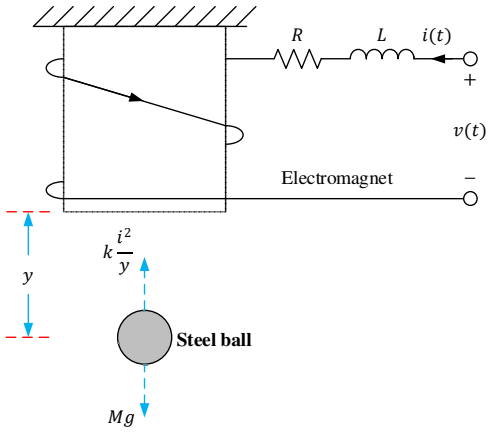

Figure 2. Magnetic levitation-based ball suspension system.

When a control voltage $v(t)$ is applied to the coil, the resulting current $i(t)$ produces a magnetic flux that generates an upward electromagnetic force proportional to ki^2/y^2, where k is the electromagnetic constant depending on the coil geometry and magnetic permeability. The gravitational force Mg acts in the opposite direction, pulling the ball downward. Consequently, the vertical motion of the ball is governed by Newton's second law, yielding the nonlinear equation of motion given in Equation (19).

$$M\ddot{y}(t) = Mg - \frac{k\,i^2(t)}{y^2(t)} \tag{19}$$

The electrical dynamics of the coil circuit are simultaneously described by the first-order differential equation:

$$v(t) = Ri(t) + L\frac{di(t)}{dt} \tag{20}$$

Equations (19) and (20) together form a nonlinear electromechanical system, coupling current and position variables. At steady state, when the ball is suspended at an equilibrium distance y_0 and the current is i_0, the electromagnetic and gravitational forces balance, i.e., $Mg = k\,i_0^2/y_0^2$. To derive a linearized model suitable for controller design, small perturbations are defined around the equilibrium point:

$$y(t) = y_0 + \Delta y(t), i(t) = i_0 + \Delta i(t), v(t) = v_0 + \Delta v(t) \tag{21}$$

Substituting (21) into (19) and (20) and neglecting higher-order terms yields the linearized state-space model that captures the local dynamics near equilibrium. Taking the Laplace transform and expressing the system in the transfer-function form gives the open-loop plant representation:

$$G_{plant}(s) = \frac{Y(s)}{V(s)} = \frac{a}{(s-p_1)(s-p_2)(s-p_3)} \tag{22}$$

where the parameters are defined as $a = -\left(\frac{2}{L}\right)\sqrt{kg/My_0} = -885.8894$, $p_1 = -\frac{R}{L} = -100$, $p_{2,3} = \pm\sqrt{g/y_0} = \pm 4.4294$. The poles $p_{2,3}$ form a pair of real roots of opposite sign, representing the inherent instability of the levitation system since one of them lies in the right-half of the s-plane [19,32–34]. Using the experimentally established parameter values [19,32–34]—$R = 1\ \Omega$, $L = 0.01$ H, $M = 1$ kg, $g = 9.81$ m/s^2, $k = 1$ kg·m^2/A^2·s^2 and $y_0 = 0.5$ m—the numerical substitution yields the linearized transfer function of the magnetic ball suspension plant, which can be written explicitly as given in Equation (23).

$$G_{plant}(s) = \frac{-885.8894}{s^3 + 100s^2 - 19.62s - 1962} \tag{23}$$

This third-order transfer function clearly demonstrates the unstable nature of the system due to the positive pole. Therefore, without feedback control, even small deviations from the equilibrium cause the ball to diverge rapidly from its suspended position. The derived model serves as the foundation for developing and tuning advanced controllers such as the FGO-optimized softsign-FOPID proposed in this work. It provides the dynamic representation required for simulating control performance, designing objective functions, and performing stability and robustness analyses.

4. Proposed Control Method

4.1. Theoretical Background and Practical Implementation of FOPID Controllers

Fractional-order control has emerged as an effective extension of classical PID theory, offering enhanced robustness and dynamic flexibility for nonlinear systems [35]. Unlike conventional PID controllers that employ first-order differentiation and integration, fractional-order PID (FOPID) models generalize these operators to real-valued orders λ and μ, which enable hereditary and memory characteristics to be reflected in the control action [36]. The fractional differentiation operator is typically defined using the Grunwald–Letnikov (G–L) framework due to its suitability for numerical implementation [37]. The β-order derivative of a function $f(t)$ over the interval $[a, t]$ is expressed as:

$$D^{\beta} f(t) = \lim_{h \to 0} \frac{1}{h^{\beta}} \sum_{r=0}^{\left[\frac{t-a}{h}\right]} (-1)^r \binom{n}{r} f(t - rh) \tag{24}$$

where $n - 1 < \beta < n$, h is the time step, and the binomial term provides fractional-order weighting [35]. This representation allows the controller to incorporate long-term past information of the error signal, strengthening noise resilience and disturbance rejection.

The transfer function of a FOPID controller is given as:

$$C_{FOPID}(s) = K_P + \frac{K_I}{s^{\lambda}} + K_D s^{\mu} \tag{25}$$

where K_P, K_I, and K_D denote the proportional, integral, and derivative gains, respectively, while λ and μ represent the fractional integral and derivative orders [38,39]. These additional degrees of freedom improve transient performance without compromising stability, especially for nonlinear and parameter-varying plants.

For real-time applications, rational approximation techniques such as discrete-time G–L implementations are widely adopted, enabling direct digital realization through finite impulse approximations [35]. This structure has already demonstrated strong robustness against dynamic uncertainties and disturbances in nonlinear power electronics and electromechanical systems, confirming its practicality and effectiveness.

In this study, the FOPID block receives the softened nonlinear error generated by the softsign function, and its contribution is tuned automatically using the FGO. The selection

of FOPID is justified by its superior disturbance rejection capability and enhanced transient shaping performance in systems characterized by strong nonlinearities such as magnetic levitation platforms.

4.2. Novel Softsign Function-Based FOPID Controller

The proposed control structure integrates a nonlinear softsign activation with a FOPID framework to achieve a smooth and adaptive control action for the magnetic ball suspension system. The complete architecture is illustrated in Figure 3, where the controller receives the position error signal $e(t)$ and produces the control output $u(t)$ through a sequence of nonlinear and fractional operations.

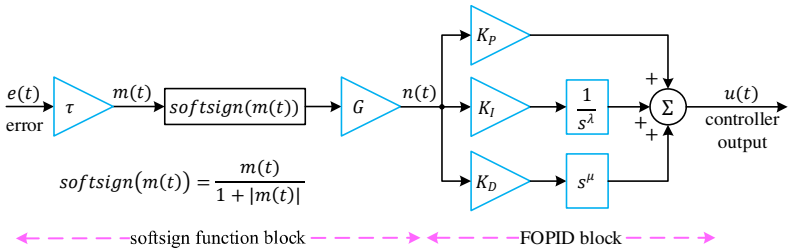

Figure 3. Architectural schematic of the proposed softsign-FOPID controller.

The transfer function of the FOPID controller has already been defined in the previous subsection by Equation (25). This generalized structure provides a wider tuning range than a conventional PID by allowing non-integer exponents that shape the frequency response more flexibly and improve robustness to parameter variations. To introduce nonlinear adaptability, the FOPID stage is preceded by a softsign function [40] block. The softsign nonlinearity is mathematically expressed as in Equation (26):

$$softsign(x) = \frac{x}{1+|x|} \tag{26}$$

which smoothly bounds large input magnitudes within the interval $(-1, +1)$. Unlike discontinuous functions, the softsign mapping preserves differentiability, ensuring continuous control action without chattering or abrupt saturation. As shown in Figure 3, the input error $e(t)$ is first scaled by a gain τ to produce an intermediate signal $m(t) = \tau \times e(t)$. This signal is then passed through the softsign nonlinearity, yielding expression in Equation (27).

$$n(t) = G \times softsign(m(t)) = G \times softsign(\tau \times e(t)) = \frac{\tau \times G \times e(t)}{1+|\tau \times e(t)|} \tag{27}$$

Here, G is an additional gain that adjusts the amplitude of the nonlinear output. The resulting signal $n(t)$ therefore represents a soft-bounded, gain-scaled version of the error, ensuring that the subsequent control stages receive a moderated input even under large tracking deviations. The signal $n(t)$ is then fed into the FOPID block, which consists of three parallel paths corresponding to the proportional, integral, and derivative terms. These branches are weighted by K_P, K_I, and K_D, respectively. The integral branch employs the fractional operator $1/s^{\lambda}$, while the derivative branch uses s^{μ}. The outputs of all three branches are summed at the node Σ to form the overall controller output $u(t)$. This cascaded design combines the benefits of both nonlinear and fractional-order control. The softsign mapping enhances stability and prevents excessive control effort, while the fractional-order dynamics allow fine control of transient and steady-state performance. Consequently, the softsign-FOPID controller achieves superior smoothness, adaptability, and robustness compared with conventional PID-type controllers.

4.3. Discussion on the Potential and Limitations of the Softsign Implementation

The introduction of the softsign function enhances the control performance by smoothly reducing the impact of large error magnitudes and preventing abrupt variations in the control action. This characteristic is particularly advantageous for the magnetic ball suspension system, where rapid error deviations may otherwise induce actuator saturation and excessive transient oscillations. The nonlinear mapping also improves the damping properties of the closed-loop dynamics by moderating the proportional and derivative responses during aggressive transients. As a result, a more stable and energy-efficient behavior is achieved during large tracking deviations and sudden reference changes.

Nevertheless, the effectiveness of the softsign activation remains dependent on appropriate coordination with the fractional orders and gain parameters of the FOPID controller. An excessively strong softsign scaling could reduce the control effort to the extent that responsiveness deteriorates, especially when rapid corrective action is required. Additionally, since the nonlinear shaping modifies the actual error delivered to the fractional branches, the selection of tuning bounds must ensure that the fractional-order dynamics preserve stability and steady-state precision. Despite these considerations, the results demonstrated in Sections 5 and 6 confirm that, when the softsign and FOPID parameters are jointly optimized by FGO, the nonlinear enhancement yields significant improvements in robustness, transient smoothness, and overshoot suppression without compromising steady-state accuracy.

4.4. Proposed Objective Function

To determine the optimal parameters of the proposed softsign-FOPID controller, a composite objective function (OF) has been formulated. The objective function integrates both transient and steady-state performance indices to ensure a well-balanced dynamic response of the magnetic ball suspension system. It is mathematically defined as minimizing the expression in Equation (28).

$$OF = \theta\left(M_p - 1\right) + (1-\theta)\int_0^{t_{sim}} |e(t)|dt \tag{28}$$

In this expression, t_{sim} represents the total simulation time, $e(t) = r(t) - y(t)$ denotes the instantaneous tracking error between the reference position $r(t)$ and the actual ball position $y(t)$, and M_p is the peak value of the ball position response. The first term, $\theta\left(M_p - 1\right)$, penalizes excessive overshoot by driving M_p close to unity, whereas the second term minimizes the accumulated absolute error throughout the simulation. By combining these two criteria, the objective function simultaneously enforces fast convergence and minimal steady-state deviation. A stability factor of $\theta = 0.1$ has been adopted to assign higher importance to the integral performance index, ensuring smoother error attenuation while maintaining control stability. The total simulation period is fixed at $t_{sim} = 5$ s, which is sufficient to capture the complete transient and settling behavior of the system. During the optimization process, the parameters of the softsign-FOPID controller are constrained within predefined practical ranges to preserve stability and realizability.

The corresponding bounds are specified as $-100 \leq K_P \leq 0$, $-100 \leq K_I \leq 0$, $-20 \leq K_D \leq 0$, $0.5 \leq \lambda \leq 1.5$, $0.5 \leq \mu \leq 1.5$, $0.2 \leq \tau \leq 10$ and $0.2 \leq G \leq 10$. Here, K_P, K_I, and K_D correspond to the proportional, integral, and derivative gains of the FOPID controller, while λ and μ denote the fractional integral and derivative orders. The parameters τ and G belong to the softsign function block and govern the scaling and amplitude of the nonlinear activation, respectively. These constraints define the feasible search space for the optimization algorithm and ensure that the resulting controller operates within

stable and implementable limits. The formulated objective function thus provides a comprehensive performance measure for tuning the softsign-FOPID controller using the fungal growth optimizer described in the subsequent section.

4.5. Implementation of the Proposed Method to the Magnetic Ball Suspension System

The integration of the FGO with the softsign-FOPID controller for the magnetic ball suspension system is schematically illustrated in Figure 4. The diagram represents the closed-loop optimization and control process, in which the controller parameters are iteratively tuned through the optimization routine until the best performance is achieved according to the defined objective function. In this implementation, the setpoint position is first compared with the measured ball position, producing the instantaneous tracking error signal. This error is then processed by the softsign-FOPID controller, whose structure has been previously described. The controller generates the control effort that drives the electromagnet to stabilize the levitated ball around its desired position.

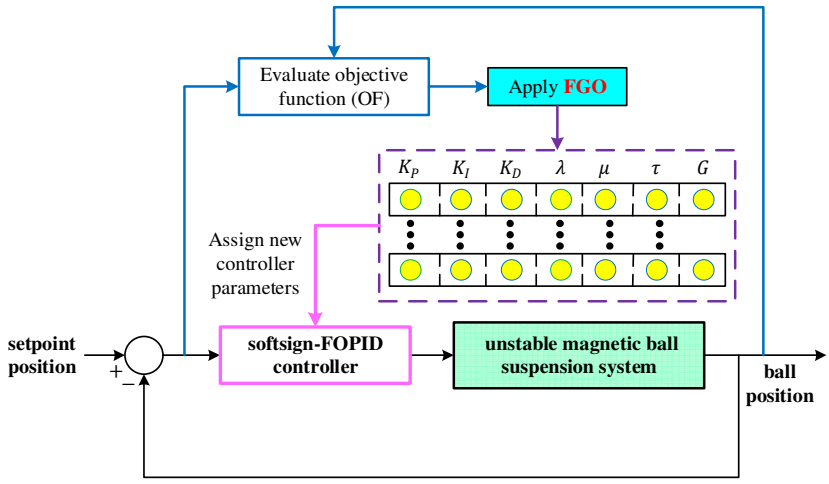

Figure 4. Implementation of the FGO-based softsign-FOPID controller to the magnetic ball suspension system.

The optimization process operates concurrently with the control loop. Initially, FGO generates a population of candidate parameter sets for the seven controller variables $[K_P, K_I, K_D, \lambda, \mu, \tau, G]$. Each candidate solution corresponds to a different tuning configuration of the softsign-FOPID controller. For every candidate, the control system is simulated, and the resulting transient response is evaluated through the objective function defined in Equation (28). The objective function computes the performance index by using the system output and the instantaneous error. The resulting objective value is then passed to the FGO, where the optimization algorithm updates the controller parameters based on the fungal growth mechanism. The newly generated parameter set is reassigned to the controller, and the process repeats until the termination criterion is met. Through this iterative tuning procedure, the FGO effectively explores the multidimensional parameter space and identifies the optimal combination of controller gains and fractional orders that minimize the objective function. The interaction between the optimizer and the control loop ensures that the system's transient and steady-state characteristics such as overshoot, rise time, and steady-state error—are simultaneously improved.

5. Results and Discussion

5.1. Compared Optimizers

To ensure a comprehensive evaluation of the proposed control approach, the performance of the FGO [31] was compared with several recently developed and well-established

metaheuristic algorithms. These include greater cane rat algorithm (GCRA) [41], catch fish optimization algorithm (CFOA) [42], RIME algorithm [43] and artificial hummingbird algorithm (AHA) [44]. Each algorithm was implemented under identical experimental conditions to guarantee a fair comparison. For all optimizers, the number of independent runs was fixed at 25 to provide reliable statistical outcomes and reduce stochastic bias. The maximum number of iterations, denoted as t_{max}, and the population size, denoted as N, were kept constant across all algorithms to maintain consistent computational effort. The remaining parameters were assigned according to the characteristic control variables of each respective algorithm as demonstrated in Table 1. By maintaining uniform iteration and population settings while preserving each algorithm's intrinsic behavioral constants, an equitable and unbiased benchmark environment was established. This ensures that the performance differences observed in subsequent analyses arise from the inherent search capabilities of the algorithms rather than from unequal parameter tuning or computational resources.

Table 1. Parameter of the compared optimizers.

Optimizer	Parameter
FGO	$t_{max} = 100,\ N = 30,\ M = 0.6,\ E_p = 0.7,\ R = 0.9$
GCRA	$t_{max} = 100,\ N = 30,\ \rho = 0.5$
CFOA	$t_{max} = 100,\ N = 30$
RIME	$t_{max} = 100,\ N = 30,\ w = 5$
AHA	$t_{max} = 100,\ N = 30,\ migration_{coefficient} = 60$

5.2. Statistical Analysis

A comprehensive statistical evaluation was conducted to assess the performance consistency and convergence quality of the compared optimization algorithms. The distribution of the obtained objective function values over 25 independent runs for each method is illustrated in Figure 5, while the corresponding numerical statistics and significance test results are summarized in Table 2. In Figure 5, the boxplot analysis visually compares the spread and central tendency of the final objective function values achieved by each metaheuristic algorithm. The red horizontal lines represent the median OF values, while the upper and lower edges of each box indicate the 75th and 25th percentiles, respectively. The whiskers denote the range of observed results, thus revealing the variability and robustness of each optimizer. From the figure, it can be clearly observed that the FGO achieved the lowest median and narrowest interquartile range among all tested algorithms, indicating superior consistency and convergence stability. In contrast, the RIME algorithm exhibited the widest distribution and highest median value, reflecting its relatively weaker optimization capability for the given problem. The AHA and GCRA algorithms demonstrated moderate performance, whereas the CFOA yielded slightly higher OF values, suggesting less efficient exploitation behavior compared with FGO.

Table 2. Statistical results and p-values obtained from nonparametric Wilcoxon's test.

Optimizer	Mean	Standard Deviation	Median	Best	Worst	p-Value
FGO	0.013812	0.00053364	0.013854	0.012950	0.014753	–
GCRA	0.015105	0.00077157	0.015074	0.014077	0.017122	2.0013×10^{-5}
CFOA	0.015655	0.00083434	0.015427	0.014407	0.017238	1.2290×10^{-5}
RIME	0.017337	0.00081552	0.017339	0.015956	0.018557	1.2290×10^{-5}
AHA	0.014799	0.00079399	0.014672	0.013697	0.016868	0.00049316

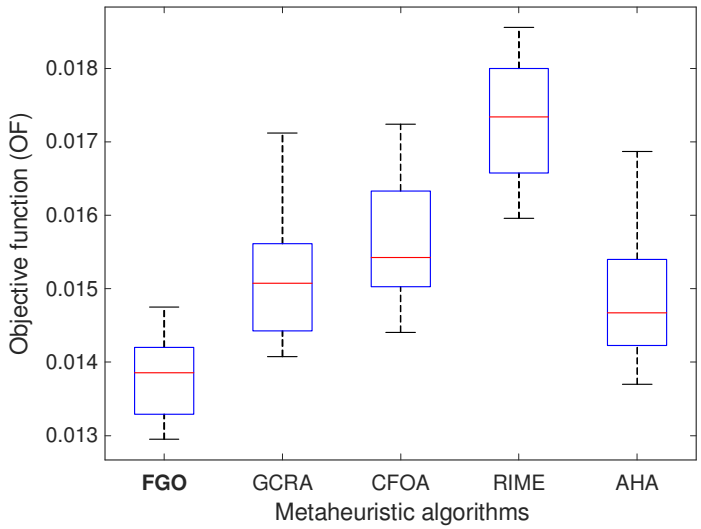

Figure 5. Comparative boxplot analysis.

The detailed statistical indicators listed in Table 2 further substantiate these visual findings. The mean, standard deviation, median, best, and worst objective values were calculated across 25 independent trials. In addition, the nonparametric Wilcoxon rank-sum test was employed to verify the statistical significance of the performance differences between FGO and the other algorithms. The results reveal that FGO produced the smallest mean objective function value (0.013812) with the lowest standard deviation (0.00053364), confirming its reliability and robustness. The *p*-values (Wilcoxon's non parametric test) [45] for all comparative tests were significantly lower than 0.05, implying that the improvements achieved by FGO are statistically significant at a 95% confidence level. Overall, both the boxplot and statistical results confirm that the FGO-based softsign-FOPID controller consistently outperformed the other optimization strategies in minimizing the objective function, thereby demonstrating its superior convergence behavior, precision, and stability across multiple independent simulations.

5.3. Minimized Objective Function Values and Obtained Controller Parameters

The convergence behavior and final optimization outcomes of the compared metaheuristic algorithms are presented in Figure 6 and Table 3, respectively. The results provide insight into both the convergence speed and the quality of the solutions achieved during the tuning of the softsign-FOPID controller parameters for the magnetic ball suspension system. In Figure 6, the comparative convergence curves illustrate the variation in the objective function value with respect to the iteration number for each optimization algorithm. It can be observed that all algorithms exhibit a general decreasing trend, confirming that each was able to effectively reduce the objective function as the iterations progressed. However, the FGO demonstrated the fastest and most stable convergence profile. It reached the minimum OF value within approximately the first 30 iterations and maintained superior stability afterward, indicating efficient exploration and exploitation balance. By contrast, the GCRA and AHA algorithms also achieved satisfactory convergence but required more iterations to reach their steady-state regions. The CFOA showed slower convergence during the initial stages, while the RIME algorithm displayed the highest residual error and the least stable convergence trajectory, implying premature stagnation and limited exploitation capacity. Overall, the convergence behavior emphasizes the robustness and rapid adaptation capability of FGO in optimizing the nonlinear and high-dimensional control problem.

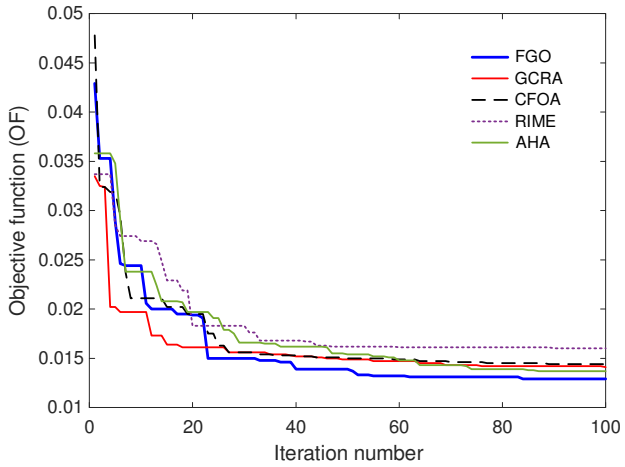

Figure 6. Comparative convergence curves.

Table 3. Obtained best controller parameters via FGO, GCRA, CFOA, RIME and AHA.

Optimizer	K_P	K_I	K_D	λ	μ	τ	G
FGO	−48.3053	−85.8977	−0.7148	1.3504	1.4998	9.6237	2.9016
GCRA	−72.0883	−98.0837	−1.2455	1.2380	1.4665	9.7256	1.7204
CFOA	−93.0335	−87.6200	−1.6623	1.1622	1.4617	9.7876	1.3481
RIME	−70.2453	−79.3388	−0.9321	1.3413	1.4359	9.9877	2.1345
AHA	−53.2461	−55.0402	−0.6548	1.2698	1.4825	9.7895	3.3240

These results confirm that the fungal growth optimizer successfully achieved the most efficient parameter set, leading to an optimal trade-off between overshoot reduction, steady-state accuracy, and control smoothness. The convergence and parameter results presented in Figure 6 and Table 3 therefore validate the superior optimization capability and stability of the FGO-based tuning strategy when applied to the magnetic ball suspension system.

The best-obtained controller parameters resulting from each optimization method are summarized in Table 3. These values correspond to the optimal configuration of the seven design variables of the softsign-FOPID controller. From the table, it is evident that all optimizers converged to feasible and stable controller settings within the defined parameter bounds. However, the parameter combination generated by FGO yielded the lowest minimized objective function value, demonstrating its superior ability to fine-tune the fractional orders (λ, μ) and the nonlinear shaping parameters (τ, G) simultaneously. Notably, the FGO-tuned controller exhibited higher values of $\lambda = 1.3504$ and $\mu = 1.4998$, indicating an increased derivative dominance that enhances responsiveness, while the moderate scaling factors $\tau = 9.6237$ and $G = 2.9016$ ensured smooth nonlinear modulation.

5.4. Step Response Analysis

The dynamic performance of the magnetic ball suspension system under different optimization algorithms was evaluated through step response tests. The comparative system responses obtained using the FGO-, GCRA-, CFOA-, RIME-, and AHA-tuned softsign-FOPID controllers are illustrated in Figure 7, with an enlarged view of the transient region provided in Figure 8. The corresponding quantitative performance indicators, namely rise time (t_{rise}), settling time (t_{set}), overshoot (OS), peak time (t_{peak}) and steady-state error (e_{ss}), are summarized in Table 4. In Figure 7, all optimized controllers achieved stable levitation and closely followed the reference setpoint. However, notable differences in transient behavior are evident among the compared algorithms. The FGO-tuned softsign-FOPID controller exhibited the smoothest response, with minimal overshoot and the fastest

stabilization, demonstrating its superior control accuracy and dynamic adaptability. The ball position reached the desired reference value almost without oscillation, confirming effective damping of transient fluctuations.

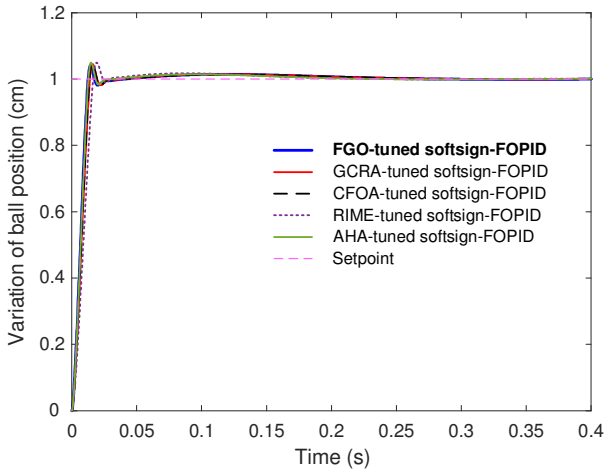

Figure 7. Comparative step response analysis for the variation in the ball position.

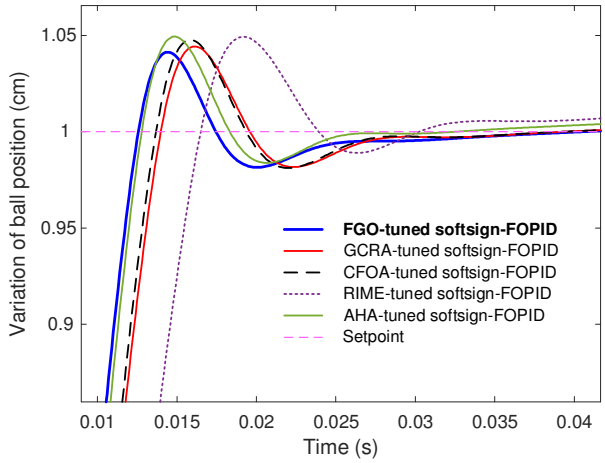

Figure 8. Enlarged view of Figure 7.

Table 4. Comparative time-domain metrics.

Optimizer	t_{rise} **(s)**	t_{set} **(s)**	OS **(%)**	t_{peak} **(s)**	e_{ss} **(%)**
FGO	0.0088566	0.016304	4.1337	0.0144	0.0015389
GCRA	0.0098480	0.018357	4.4302	0.0161	0.0053397
CFOA	0.0096376	0.018201	4.7731	0.0158	0.0083288
RIME	0.0116480	0.022285	4.9301	0.0192	0.0069259
AHA	0.0090177	0.017182	4.9377	0.0148	0.0075042

The enlarged transient region in Figure 8 highlights the fine distinctions among the responses. The FGO-based controller reached the target position more rapidly and exhibited the lowest overshoot magnitude, while maintaining a nearly negligible steady-state error. The GCRA and AHA controllers produced slightly higher overshoot values but still achieved fast convergence, whereas the CFOA and RIME controllers showed relatively slower rise and settling times, indicating less efficient transient shaping. The performance superiority of the FGO-based tuning approach thus becomes evident, particularly in terms of balancing rapid response and overshoot minimization.

From the tabulated results, the FGO-based controller achieved the fastest rise time (0.0088566 s) and shortest settling time (0.016304 s), while maintaining the lowest steady-state error and one of the smallest overshoot values. The RIME algorithm, by contrast, produced the largest rise and settling times, signifying slower response dynamics. The close agreement between the GCRA and AHA results indicates that both algorithms performed moderately well, though they lagged slightly behind FGO in precision. Overall, the comparative results from Figures 7 and 8 and Table 4 demonstrate that the FGO-tuned softsign-FOPID controller yields the most desirable transient characteristics—combining rapid response, low overshoot, and high steady-state accuracy. This confirms the efficiency of the fungal growth optimizer in fine-tuning nonlinear fractional-order controllers for complex unstable systems such as the magnetic ball suspension platform.

5.5. Comparisons with the Reported Best Approaches

To further validate the performance superiority of the proposed control framework, the FGO-tuned softsign-FOPID controller was benchmarked against several high-performing controllers previously reported in the literature: the sine cosine algorithm (SCA)-tuned PID [33], logarithmic spiral opposition-based learning augmented hunger games search algorithm (LsOBL-HGS)-tuned FOPID [34], and manta ray foraging optimization (MRFO)-tuned real PIDD^2 [19]. The comparative step responses are shown in Figure 9, and the corresponding time-domain performance metrics are summarized in Table 5. In Figure 9, the step responses reveal marked differences in transient and steady-state behavior among the four controllers. The proposed FGO-tuned softsign-FOPID exhibits the fastest rise and settling times with minimal overshoot, achieving a smooth and well-damped trajectory that closely tracks the reference setpoint. The SCA-tuned PID displays the largest overshoot (25%) and a considerably longer settling period, highlighting the limitations of integer-order control for this highly nonlinear magnetic levitation system. The LsOBL-HGS-tuned FOPID achieves better damping than the PID controller but still suffers from a noticeably higher overshoot (12.79%) and slower convergence. The MRFO-tuned real PIDD^2 provides an improvement over SCA and LsOBL-HGS in terms of rise and settling times, yet its response remains less stable and more oscillatory compared with the FGO-based design.

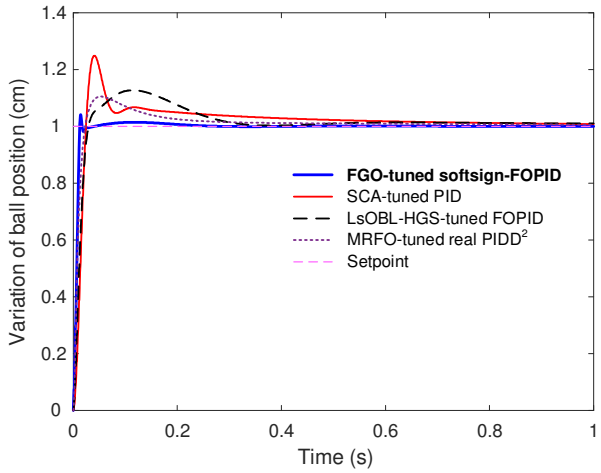

Figure 9. Step response performance of the proposed method with respect to reported approaches.

The results clearly indicate that the FGO-tuned softsign-FOPID controller achieved the shortest rise time (0.0089 s), fastest settling time (0.0163 s), and lowest overshoot (4.13%), while maintaining an extremely small steady-state error ($e_{ss} = 0.0015\%$). In contrast, the PID, FOPID, and PIDD^2 controllers tuned via SCA, LsOBL-HGS, and MRFO, respectively, exhibited notably longer response times and greater overshoots. These findings underscore

that the proposed softsign-FOPID design, optimized via the fungal growth optimizer, provides a remarkable enhancement in control precision and transient performance compared with the best existing techniques. The combination of fractional-order dynamics and nonlinear softsign activation, coupled with the adaptive search behavior of FGO, enables the controller to outperform both conventional and advanced metaheuristic-based designs reported in prior studies.

Table 5. Comparative time-domain performance analysis with respect to reported best approaches.

Optimizer	Controller Type	Reference	t_{rise} (s)	t_{set} (s)	OS (%)	t_{peak} (s)	e_{ss} (%)
FGO	softsign-FOPID	Proposed	0.0088566	0.016304	4.1337	0.0144	0.0015389
SCA	Ideal PID	[33]	0.016812	0.55059	24.875	0.0407	0.00045351
LsOBL-HGS	FOPID	[34]	0.020721	0.28488	12.786	0.1143	0.25575
MRFO	Real PIDD^2	[19]	0.014496	0.23292	10.482	0.0534	0.008617

6. Evaluation of Control Effectiveness Under Practical Non-Idealities

To validate the robustness and real-world applicability of the proposed control framework, the FGO-tuned softsign-FOPID controller was further tested under various practical non-ideal conditions, including actuator saturation, sensor noise, and external disturbances. The simulation setup used for this analysis is illustrated in Figure 10, which depicts the complete closed-loop configuration employed to assess the controller's resilience to these non-idealities. As shown in the figure, the setpoint position, denoted as $R(s)$, represents the desired vertical position of the levitated ball. The difference between the reference input and the measured output $Y(s)$ produces the error signal, $E(s) = R(s) - Y(s)$, which is processed by the FGO-tuned softsign-FOPID controller. This controller dynamically generates the control action based on the nonlinear fractional-order structure optimized through the fungal growth algorithm, as previously discussed in Sections 4 and 5.

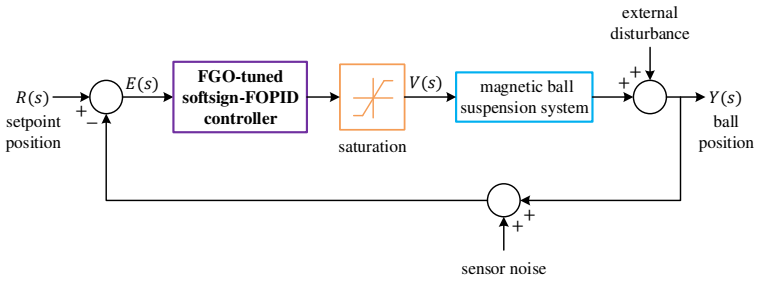

Figure 10. The setup for the evaluation of the proposed control method for the non-idealities.

The resulting control signal, $U(s)$, passes through a saturation block that emulates the physical voltage or current limitations of the electromagnetic actuator. This nonlinearity ensures that the simulated control input does not exceed realistic operational bounds, thereby reflecting the behavior of the actual magnetic suspension hardware. The magnetic ball suspension system receives the saturated control input and produces the actual ball position response, $Y(s)$. To represent the unpredictable conditions encountered in real environments, two major disturbances are introduced into the feedback loop: (1) external disturbance, acting directly on the magnetic actuator output or ball position, simulates external vibrations or air currents that can momentarily alter the levitation stability and (2) sensor noise, added to the feedback measurement path, models the random fluctuations and measurement inaccuracies that typically occur in practical sensing hardware. These perturbations are depicted in Figure 10 as additive inputs entering the feedback loop at different points; external disturbance applied at the actuator output and sensor noise added

to the measured position signal. The combined influence of these effects provides a realistic and comprehensive test environment for evaluating the proposed control strategy.

Through this experimental setup, the effectiveness of the FGO-optimized softsign-FOPID controller can be analyzed not only in terms of nominal system performance but also in its ability to maintain stability, precision, and smoothness under noisy, constrained, and disturbed conditions. The subsequent subsections present detailed analyses of the controller's behavior under fluctuating reference positions, actuator saturation with external disturbance and sensor noise, and parametric uncertainties, demonstrating its robustness and practical reliability.

6.1. Under Fluctuating Reference Positions

To assess the tracking capability and adaptability of the proposed controller, the FGO-tuned softsign-FOPID was evaluated under time-varying reference inputs. Unlike conventional step commands, the reference trajectory in this test consists of continuously changing and randomly fluctuating position signals to emulate real-world operational scenarios where the target levitation height varies dynamically. The system's corresponding response is illustrated in Figure 11. As shown in the figure, the blue curve represents the actual variation in the ball position governed by the FGO-optimized softsign-FOPID controller, while the red dashed curve denotes the randomly fluctuating reference input. Throughout the entire 17 s simulation period, the controlled response accurately follows the reference signal with negligible phase lag and minimal amplitude deviation. This close overlap between the reference and response trajectories demonstrates the strong tracking precision and adaptive nature of the proposed controller.

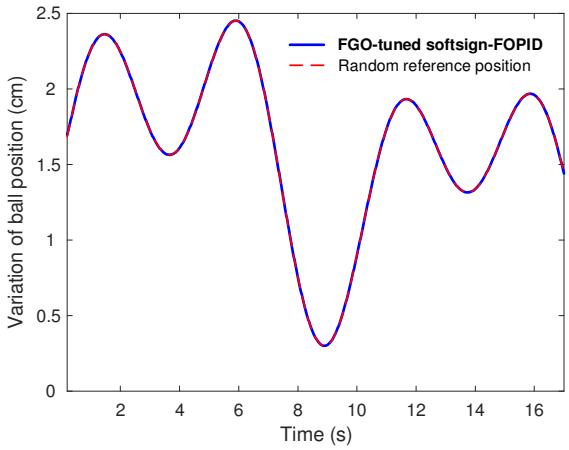

Figure 11. Performance analysis for fluctuating reference positions.

Even during abrupt reference changes and high-frequency variations, the control signal maintains smoothness without noticeable overshoot or oscillatory divergence. The fractional-order dynamics, combined with the softsign nonlinear activation, enable the controller to dynamically modulate its corrective effort according to the instantaneous rate of change of the input signal. Consequently, the magnetic levitation system remains stable and responsive despite rapid target fluctuations. The results clearly indicate that the proposed FGO-tuned softsign-FOPID controller possesses superior adaptability and robustness in tracking variable reference positions. Its effective balance between fast transient response and stability ensures continuous levitation control performance under non-stationary operating conditions which is an essential requirement for practical magnetic suspension and precision positioning applications.

6.2. Under Actuator Saturation, External Disturbance, and Sensor Noise

In addition to fluctuating reference tracking, the robustness of the FGO-tuned softsign-FOPID controller was evaluated under multiple real-world non-idealities, namely actuator saturation, external disturbances, and sensor noise. This analysis was conducted to verify the controller's ability to maintain accurate levitation performance when exposed to practical constraints and unpredictable external effects. The corresponding results are illustrated in Figure 12. In this simulation, the setpoint (depicted by the red dashed line) represents the desired equilibrium position of the magnetic ball, while the blue curve shows the actual system response governed by the proposed controller. Two main disturbance types were introduced during operation: (1) external disturbances were applied directly to the system output to simulate sudden perturbations such as air gusts or electromagnetic fluctuations and (2) sensor noise was added to the feedback loop to emulate high-frequency measurement noise originating from practical sensing hardware. Furthermore, a saturation nonlinearity was incorporated into the actuator model to restrict the control signal amplitude, ensuring that the simulated system adhered to realistic current and voltage limitations of the electromagnetic coil.

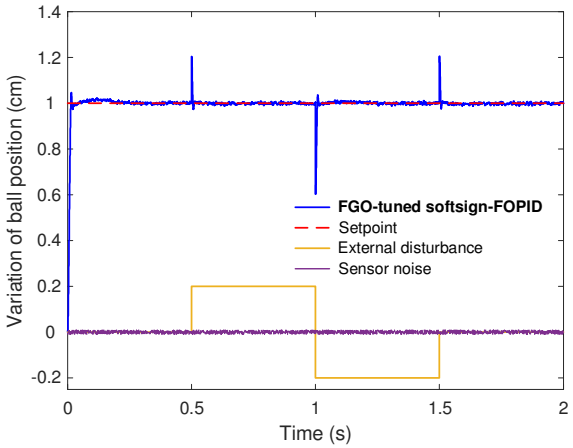

Figure 12. Performance analysis of the proposed method for the actuator saturation, external disturbances and sensor noise.

As observed in Figure 12, the system maintained excellent stability and precise position control despite these simultaneous non-ideal conditions. When external disturbances occurred, small transient spikes appeared momentarily in the ball position, but the controller rapidly suppressed them and restored the system to its equilibrium within milliseconds. The smooth response indicates that the proposed control method effectively compensated for the actuator saturation and disturbance effects without introducing sustained oscillations or offset. The presence of sensor noise had negligible influence on the output trajectory, demonstrating the controller's strong filtering capability. This robustness can be attributed to the synergistic structure of the softsign-FOPID controller, where the nonlinear softsign function limits abrupt control variations while the fractional-order dynamics provide flexible damping and memory properties. The optimized parameters obtained via the fungal growth optimizer (FGO) further ensure balanced adaptability between responsiveness and stability under uncertain conditions. In summary, the performance analysis presented in Figure 12 confirms that the FGO-tuned softsign-FOPID controller exhibits outstanding robustness and resilience against actuator limitations, environmental disturbances, and measurement noise. These results validate its suitability for real-time magnetic levitation control, where precision and reliability must be preserved even under practical system imperfections.

To provide a comprehensive evaluation of the derivative action behavior, the controller output of the FGO-tuned softsign-FOPID structure has been visualized under noisy measurement conditions and disturbance events. The resulting transient output signal is depicted in Figure 13. The recorded control effort remains bounded throughout operation, confirming that the nonlinear softsign activation effectively moderates high-magnitude variations. Although isolated peaks occur during abrupt disturbance changes, such transient deviations diminish rapidly and do not evolve into sustained high-frequency oscillations. This desirable behavior is attributed to the first-order derivative filtering embedded in the FOPID structure through the FOMCON toolbox [46] implementation, where a derivative filter time constant of 0.0001 s, an approximation order of 5, and a frequency range of $[10^{-4}, 10^{4}]$ were selected. This filtering approach limits noise amplification and prevents excessive actuator activity while preserving the beneficial responsiveness of the derivative term. These findings confirm the practical viability of the proposed control strategy, achieving robust stabilization without compromising actuator health or long-term reliability.

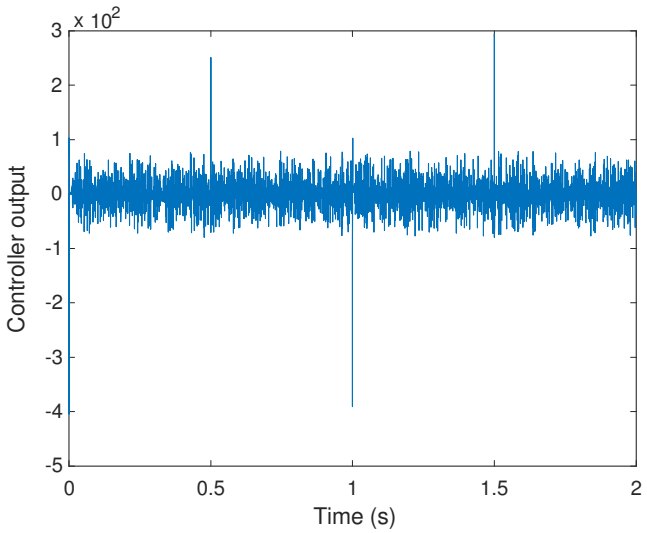

Figure 13. Transient response of FGO-tuned softsign-FOPID controller output.

6.3. Robustness Characterization Under Parametric Uncertainties

To further validate the stability and reliability of the proposed control strategy, a robustness analysis was conducted by introducing parametric uncertainties into the magnetic ball suspension system model. This analysis examined the controller's ability to maintain performance when key system parameters deviated from their nominal values, simulating manufacturing tolerances, environmental variations, or aging effects in the physical components. The parameter configurations adopted for this investigation are summarized in Table 6, while the corresponding system responses are illustrated in Figure 14. In this study, the coil resistance (R) and inductance (L) were selected as the uncertain parameters, as they directly influence the electromagnetic force generation and dynamic response of the levitation system. Four perturbed scenarios were defined around the nominal configuration as shown in Table 6.

Table 6. Different parameter settings adopted for the robustness analysis.

System Parameter	Nominal	Case (a)	Case (b)	Case (c)	Case (d)
R	1	0.9	1.1	1	1
L	0.01	0.01	0.01	0.009	0.011

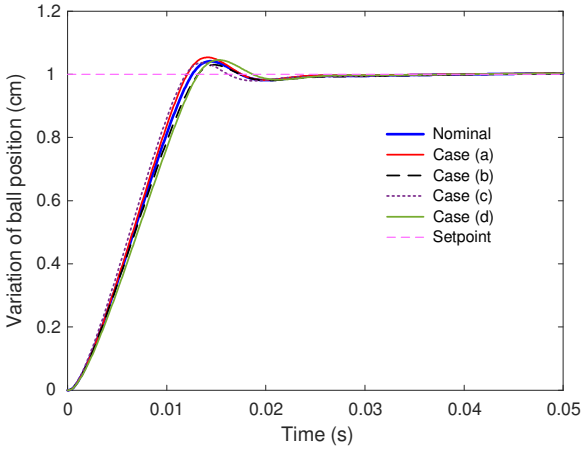

Figure 14. Robustness analysis for different cases.

The resulting step responses for these cases are shown in Figure 14, along with the nominal system behavior for reference. As illustrated in the figure, all perturbed cases closely follow the nominal trajectory, with only minor deviations observed during the transient phase. The FGO-tuned softsign-FOPID controller successfully maintained system stability and ensured consistent dynamic performance across all uncertainty scenarios. Despite variations in the electromagnetic parameters, the overshoot, settling time, and steady-state accuracy remained virtually unchanged, highlighting the robustness of the control design. Specifically, slight increases or decreases in resistance and inductance caused negligible shifts in the rise and peak times but did not lead to oscillations or divergence. The softsign nonlinear mapping contributed to this robustness by preventing excessive control effort under altered dynamic conditions, while the fractional-order elements provided inherent adaptability through memory-based error correction. This combination ensured stable levitation control even when the system's electrical characteristics were significantly perturbed. Overall, the robustness characterization presented in Figure 14 confirms that the FGO-optimized softsign-FOPID controller maintains excellent performance and resilience under parameter uncertainties. The controller's adaptive structure and optimally tuned fractional orders enable it to preserve control precision and transient quality without requiring retuning, thereby demonstrating strong suitability for real-world applications of magnetic levitation systems operating under uncertain or variable physical conditions.

7. Conclusions

In this study, a novel softsign-FOPID controller was proposed and optimized using the recently developed FGO to achieve high-precision and robust control of an unstable magnetic ball suspension system. The research successfully integrated nonlinear control, fractional calculus, and metaheuristic optimization into a unified framework capable of handling the system's inherent instability, nonlinearities, and sensitivity to parameter variations. The proposed controller architecture combined the fractional-order PID structure with a softsign nonlinear activation, which introduced a smooth, bounded control effort while maintaining fast dynamic adaptability. This structure effectively mitigated overshoot and chattering issues typically associated with nonlinear controllers and enhanced damping during transient responses. The FGO algorithm was employed to determine the optimal controller parameters by minimizing a composite objective function (OF) that simultaneously considered overshoot suppression and cumulative error minimization. The optimizer's adaptive balance between exploration and exploitation enabled rapid convergence toward globally optimal solutions with high consistency across multiple independent runs. Comprehensive comparative analyses were carried out against four

advanced metaheuristic algorithms (GCRA, CFOA, RIME, and AHA) under identical optimization settings. The statistical results and boxplot comparisons demonstrated that FGO consistently achieved the lowest mean and variance of the objective function, as confirmed by Wilcoxon rank-sum tests with statistically significant improvements ($p < 0.05$). The convergence characteristics further validated FGO's superior efficiency and stability during parameter tuning. Time-domain performance assessments indicated that the FGO-tuned softsign-FOPID controller provided the fastest rise time, shortest settling time, and lowest overshoot, outperforming all compared methods. When benchmarked against the best previously reported controllers (namely the SCA-tuned PID, LsOBL-HGS-tuned FOPID, and MRFO-tuned real PIDD^2), the proposed controller exhibited superior transient and steady-state performance, confirming its advancement beyond the state of the art in magnetic levitation control. The robustness and practical viability of the proposed control strategy were further validated under several non-ideal operating conditions. The controller maintained excellent performance when subjected to fluctuating reference trajectories, actuator saturation, sensor noise, and external disturbances. Additionally, the robustness characterization under parameter uncertainties demonstrated that even with $\pm 10\%$ variations in resistance and inductance, the closed-loop system remained stable with negligible degradation in transient behavior. These results collectively confirm that the FGO-tuned softsign-FOPID controller possesses strong resilience, adaptability, and precision under realistic implementation constraints. In summary, the proposed FGO-based softsign-FOPID control framework provides a significant improvement over existing control and optimization strategies for magnetic suspension systems. Its design successfully combines the smooth nonlinearity of the softsign function with the memory and flexibility of fractional-order dynamics, optimized through an intelligent, nature-inspired algorithm. The resulting controller exhibits high control precision, rapid convergence, and remarkable robustness, making it a promising candidate for broader applications in nonlinear, unstable, and noise-sensitive systems.

Author Contributions: Conceptualization, S.E.; methodology, D.I.; software, D.I.; validation, D.I., and S.E.; formal analysis, D.I. and M.A.A.; investigation, D.I.; resources, D.I.; data curation, D.I. and S.E.; writing—original draft preparation, D.I. and S.E.; writing—review and editing, M.Z.M.T. and M.A.A.; visualization, M.Z.M.T.; supervision, S.E.; project administration, S.E.; funding acquisition, M.A.A. All authors have read and agreed to the published version of the manuscript.

Funding: This research was funded by MTUN Strategic Collaboration Research Grant, RDU243501.

Data Availability Statement: All produced data are available within the manuscript.

Acknowledgments: The highest gratitude is especially extended to the Universiti Malaysia Pahang Al-Sultan Abdullah for the financial assistance provided under the MTUN Strategic Collaboration Research Grant, RDU243501.

Conflicts of Interest: The authors declare no conflicts of interest.

Abbreviations

The following abbreviations are used in this manuscript:

ANFISs	Adaptive neuro-fuzzy inference systems
AHA	Artificial hummingbird algorithm
CFOA	Catch fish optimization algorithm
DE	Differential evolution
FGO	Fungal growth optimizer
FOPID	Fractional-order PID

GA	Genetic algorithm
GCRA	Greater cane rat algorithm
HGS	Hunger games search
MBS	Magnetic-ball suspension
MPC	Model-predictive control
MRAC	Model-reference adaptive control
MRFO	Manta ray foraging optimization
PID	Proportional–integral–derivative
PIDA	Proportional–integral–derivative–acceleration
PSO	Particle swarm optimization
SMC	Sliding-mode control

References

1. Zhu, Q.; Wang, S.-M.; Ni, Y.-Q. A Review of Levitation Control Methods for Low- and Medium-Speed Maglev Systems. *Buildings* **2024**, *14*, 837. [CrossRef]
2. Dey, S.; Banerjee, S.; Dey, J. Design of an Improved Robust Fractional Order PID Controller for Magnetic Levitation System Based on Atom Search Optimization. *Sādhanā* **2022**, *47*, 188. [CrossRef]
3. Swain, S.K.; Sain, D.; Mishra, S.K.; Ghosh, S. Real Time Implementation of Fractional Order PID Controllers for a Magnetic Levitation Plant. *AEU—Int. J. Electron. Commun.* **2017**, *78*, 141–156. [CrossRef]
4. Chopade, A.S.; Khubalkar, S.W.; Junghare, A.S.; Aware, M.V.; Das, S. Design and Implementation of Digital Fractional Order PID Controller Using Optimal Pole-Zero Approximation Method for Magnetic Levitation System. *IEEE/CAA J. Autom. Sin.* **2018**, *5*, 977–989. [CrossRef]
5. Khan, M.K.A.A.; Manzoor, S.; Marais, H.; Aramugam, K.; Elamvazuthi, I.; Parasuraman, S. PID Controller Design for a Magnetic Levitation System. In Proceedings of the 2018 IEEE 4th International Symposium in Robotics and Manufacturing Automation (ROMA), Perambalur, India, 10–12 December 2018; pp. 1–5.
6. Wei, W.; Yu, S.; Li, B. Research on Magnetic Characteristics and Fuzzy PID Control of Electromagnetic Suspension. *Actuators* **2023**, *12*, 203. [CrossRef]
7. Monje, C.A.; Chen, Y.; Vinagre, B.M.; Xue, D.; Feliu, V. *Fractional-Order Systems and Controls*; Springer: London, UK, 2010; ISBN 978-1-84996-334-3.
8. Mughees, A.; Mughees, N.; Mughees, A.; Mohsin, S.A.; Ejsmont, K. Enhancing Stability and Position Control of a Constrained Magnetic Levitation System through Optimal Fractional-Order PID Controller. *Alex. Eng. J.* **2024**, *107*, 730–746. [CrossRef]
9. Jaiswal, S.; Suresh Kumar, C.; Seepana, M.M.; Babu, G.U.B. Design of Fractional Order PID Controller Using Genetic Algorithm Optimization Technique for Nonlinear System. *Chem. Product. Process Model.* **2020**, *15*, 20190072. [CrossRef]
10. Lin, J.; Cheng, K.W.E.; Zhang, Z.; Cheung, N.C.; Xue, X. Adaptive Sliding Mode Technique-based Electromagnetic Suspension System with Linear Switched Reluctance Actuator. *IET Electr. Power Appl.* **2015**, *9*, 50–59. [CrossRef]
11. Huang, K.; Zhang, Y.; Yu, F. Predictive Controller Design for Electromagnetic Suspension Based on Mixed Logical Dynamical Model. *J. Vib. Control* **2012**, *18*, 1165–1176. [CrossRef]
12. Chen, S.-C.; Nguyen, V.-S.; Le, D.-K.; Hsu, M.-M. ANFIS Controller for an Active Magnetic Bearing System. In Proceedings of the 2013 IEEE International Conference on Fuzzy Systems (FUZZ-IEEE), Hyderabad, India, 7–10 July 2013; pp. 1–8.
13. Wai, R.-J.; Lee, J.-D. Adaptive Fuzzy-Neural-Network Control for Maglev Transportation System. *IEEE Trans. Neural Netw.* **2008**, *19*, 54–70. [CrossRef]
14. Al Mashhadany, Y.I.; Lilo, M.A.; Abbas, A.K. Study and Analysis of Magnetic Levitation System via ANFIS Controller. *AIP Conf. Proc.* **2022**, *2400*, 040007. [CrossRef]
15. Vimala, S.A.; Sathiyavathi, S. Design of Sliding Mode Controller for Magnetic Levitation System. *Comput. Electr. Eng.* **2019**, *78*, 184–203. [CrossRef]
16. Jumaa Alkurawy, L.E.; Mohammed, K.G. Model Predictive Control of Magnetic Levitation System. *Int. J. Electr. Comput. Eng. (IJECE)* **2020**, *10*, 5802. [CrossRef]
17. Gopi, R.S.; Srinivasan, S.; Panneerselvam, K.; Teekaraman, Y.; Kuppusamy, R.; Urooj, S. Enhanced Model Reference Adaptive Control Scheme for Tracking Control of Magnetic Levitation System. *Energies* **2021**, *14*, 1455. [CrossRef]
18. Shawki, N.; Alam, S.; Sen Gupta, A.K. Design and Implementation of a Magnetic Levitation System Using Phase Lead Compensation Technique. In Proceedings of the 2014 9th International Forum on Strategic Technology (IFOST), Cox's Bazar, Bangladesh, 21–23 October 2014; pp. 294–299.
19. Ekinci, S.; Izci, D.; Kayri, M. An Effective Controller Design Approach for Magnetic Levitation System Using Novel Improved Manta Ray Foraging Optimization. *Arab. J. Sci. Eng.* **2022**, *47*, 9673–9694. [CrossRef]

20. Ghosh, A.; Rakesh Krishnan, T.; Tejaswy, P.; Mandal, A.; Pradhan, J.K.; Ranasingh, S. Design and Implementation of a 2-DOF PID Compensation for Magnetic Levitation Systems. *ISA Trans.* **2014**, *53*, 1216–1222. [CrossRef]
21. Mughees, A.; Mohsin, S.A. Design and Control of Magnetic Levitation System by Optimizing Fractional Order PID Controller Using Ant Colony Optimization Algorithm. *IEEE Access* **2020**, *8*, 116704–116723. [CrossRef]
22. Dey, S.; Dey, J.; Banerjee, S. Optimization Algorithm Based PID Controller Design for a Magnetic Levitation System. In Proceedings of the 2020 IEEE Calcutta Conference (CALCON), Kolkata, India, 28–29 February 2020; pp. 258–262.
23. Belmonte, L.M.; Segura, E.; Fernández-Caballero, A.; Somolinos, J.A.; Morales, R. Generalised Proportional Integral Control for Magnetic Levitation Systems Using a Tangent Linearisation Approach. *Mathematics* **2021**, *9*, 1424. [CrossRef]
24. Unni, A.C.; Junghare, A.S.; Mohan, V.; Ongsakul, W. PID, Fuzzy and LQR Controllers for Magnetic Levitation System. In Proceedings of the 2016 International Conference on Cogeneration, Small Power Plants and District Energy (ICUE), Bangkok, Thailand, 14–16 September 2016; pp. 1–5.
25. Humaidi, A.J.; Badr, H.M.; Hameed, A.H. PSO-Based Active Disturbance Rejection Control for Position Control of Magnetic Levitation System. In Proceedings of the 2018 5th International Conference on Control, Decision and Information Technologies (CoDIT), Thessaloniki, Greece, 10–13 April 2018; pp. 922–928.
26. Ahmad, I.; Shahzad, M.; Palensky, P. Optimal PID Control of Magnetic Levitation System Using Genetic Algorithm. In Proceedings of the 2014 IEEE International Energy Conference (ENERGYCON), Cavtat, Croatia, 13–16 May 2014; pp. 1429–1433.
27. Jastrzebski, R.P.; Jaatinen, P.; Pyrhonen, O.; Chiba, A. Design Optimization of Permanent Magnet Bearingless Motor Using Differential Evolution. In Proceedings of the 2018 IEEE Energy Conversion Congress and Exposition (ECCE), Portland, OR, USA, 23–27 September 2018; pp. 2327–2334.
28. Izci, D.; Ekinci, S.; Eker, E.; Kayri, M. A Novel Modified Opposition-based Hunger Games Search Algorithm to Design Fractional Order Proportional-integral-derivative Controller for Magnetic Ball Suspension System. *Adv. Control Appl.* **2022**, *4*, e96. [CrossRef]
29. Tepljakov, A.; Alagoz, B.B.; Yeroglu, C.; Gonzalez, E.A.; Hosseinnia, S.H.; Petlenkov, E.; Ates, A.; Cech, M. Towards Industrialization of FOPID Controllers: A Survey on Milestones of Fractional-Order Control and Pathways for Future Developments. *IEEE Access* **2021**, *9*, 21016–21042. [CrossRef]
30. Yadav, S.; Verma, S.K.; Nagar, S.K. Performance Enhancement of Magnetic Levitation System Using Teaching Learning Based Optimization. *Alex. Eng. J.* **2018**, *57*, 2427–2433. [CrossRef]
31. Abdel-Basset, M.; Mohamed, R.; Abouhawwash, M. Fungal Growth Optimizer: A Novel Nature-Inspired Metaheuristic Algorithm for Stochastic Optimization. *Comput. Methods Appl. Mech. Eng.* **2025**, *437*, 117825. [CrossRef]
32. Golnaraghi, F.; Kuo, B.C. *Automatic Control Systems*, 8th ed.; McGraw-Hill Education: London, UK, 2017; ISBN 1259643832.
33. Ozaydin, C.; Zeynelgil, H.L.; Ekinci, S.; Hekimoglu, B. PID Controller Design Based on Sine Cosine Algorithm for Magnetic Ball Suspension System. In Proceedings of the 2019 International Conference on Artificial Intelligence and Data Processing Symposium, IDAP 2019, Malatya, Turkey, 21–22 September 2019; pp. 1–7.
34. Izci, D.; Ekinci, S.; Eker, E.; Kayri, M. Augmented Hunger Games Search Algorithm Using Logarithmic Spiral Opposition-Based Learning for Function Optimization and Controller Design. *J. King Saud Univ.—Eng. Sci.* **2024**, *36*, 330–338. [CrossRef]
35. Izci, D.; Ekinci, S. A Novel Improved Version of Hunger Games Search Algorithm for Function Optimization and Efficient Controller Design of Buck Converter System. *e-Prime—Adv. Electr. Eng. Electron. Energy* **2022**, *2*, 100039. [CrossRef]
36. Izci, D.; Ekinci, S. A Novel-Enhanced Metaheuristic Algorithm for FOPID-Controlled and Bode's Ideal Transfer Function–Based Buck Converter System. *Trans. Inst. Meas. Control* **2023**, *45*, 1854–1872. [CrossRef]
37. Shah, P.; Agashe, S. Review of Fractional PID Controller. *Mechatronics* **2016**, *38*, 29–41. [CrossRef]
38. Ekinci, S.; Izci, D.; Gider, V.; Abualigah, L.; Bajaj, M.; Zaitsev, I. Optimized FOPID Controller for Steam Condenser System in Power Plants Using the Sinh-Cosh Optimizer. *Sci. Rep.* **2025**, *15*, 6876. [CrossRef]
39. Abualigah, L.; Ekinci, S.; Izci, D.; Zitar, R.A. Modified Elite Opposition-Based Artificial Hummingbird Algorithm for Designing FOPID Controlled Cruise Control System. *Intell. Autom. Soft Comput.* **2023**, *38*, 169–183. [CrossRef]
40. Pham, L.T.; Oksum, E.; Van Le, D.; Ferreira, F.J.F.; Le, S.T. Edge Detection of Potential Field Sources Using the Softsign Function. *Geocarto Int.* **2022**, *37*, 4255–4268. [CrossRef]
41. Agushaka, J.O.; Ezugwu, A.E.; Saha, A.K.; Pal, J.; Abualigah, L.; Mirjalili, S. Greater Cane Rat Algorithm (GCRA): A Nature-Inspired Metaheuristic for Optimization Problems. *Heliyon* **2024**, *10*, e31629. [CrossRef] [PubMed]
42. Jia, H.; Wen, Q.; Wang, Y.; Mirjalili, S. Catch Fish Optimization Algorithm: A New Human Behavior Algorithm for Solving Clustering Problems. *Clust. Comput.* **2024**, *27*, 13295–13332. [CrossRef]
43. Su, H.; Zhao, D.; Heidari, A.A.; Liu, L.; Zhang, X.; Mafarja, M.; Chen, H. RIME: A Physics-Based Optimization. *Neurocomputing* **2023**, *532*, 183–214. [CrossRef]
44. Zhao, W.; Wang, L.; Mirjalili, S. Artificial Hummingbird Algorithm: A New Bio-Inspired Optimizer with Its Engineering Applications. *Comput. Methods Appl. Mech. Eng.* **2022**, *388*, 114194. [CrossRef]

45. Cong, X.; Hartings, J.A.; Rao, M.B.; Jandarov, R.A. A Count Weighted Wilcoxon Rank-Sum Test and Application to Medical Data. *Commun. Stat. Simul. Comput.* **2025**, *54*, 1360–1370. [CrossRef]
46. Tepljakov, A. Toolbox. In *Fractional-Order Modeling and Control of Dynamic Systems*; Springer: Berlin/Heidelberg, Germany, 2017; pp. 107–129.